Computers and Fluids 214 (2021) 104776

Contents lists available at ScienceDirect

Computers and Fluids

journal homepage: www.elsevier.com/locate/compfluid

Application of half-way approach to discrete unified gas kinetic scheme for simulating pore-scale porous media flows

Shi Tao[a,*], Liang Wang[b], Ya Ge[a], Qing He[a,*]

[a] Key Laboratory of Distributed Energy Systems of Guangdong Province, Dongguan University of Technology, Dongguan 523808, China
[b] School of Energy Power and Mechanical Engineering, North China Electric Power University, Beijing 102206, China

ARTICLE INFO

Article history:
Received 21 March 2020
Revised 25 July 2020
Accepted 27 October 2020
Available online 30 October 2020

Keywords:
Discrete unified gas kinetic scheme
Half-way approach
Ghost-cell method
Porous media flow
Pore-scale simulation

ABSTRACT

Simulation of pore-scale porous media flows is generally considered to be a non-trivial task due to the complicacy of geometry structures involved. In the recent decades, the mesoscopic scheme of lattice Boltzmann equation (LBE), combined with the inherent half-way (HW) bounce-back boundary method has been proved to efficiently handle those complex flows. More recently, a new mesoscopic method called discrete unified gas kinetic scheme (DUGKS) is proposed in the literature, which is partially derived from the LBE. In view of that, the HW-type boundary approach is introduced to the DUGSK in this study, which is accomplished within the framework of the ghost-cell (GC) method. The HWGC-DUGKS is then developed for extending the application of DUGKS to the complex flows in the porous media. The simulations of the cylindrical Couette flow, flow through a square array of cylinders and flow in the random porous media are performed to validate the present HWGC-DUGKS. The results demonstrate the accuracy and feasibility of the method for pore-scale porous media flows, and the non-uniform mesh and rarefied effect can be conveniently incorporated into the method.

© 2020 Elsevier Ltd. All rights reserved.

1. Introduction

Porous media flows have received much attention because of their wide application in the energy, environment, chemical engineering and other fields. Particularly, the pore-scale modeling [1],[2] is capable of unveiling the flow mechanism in porous media and exploring unknown flow patterns at pore scale, and hence is expected to play an increasingly significant role in the investigation of porous media flows. Contrary to the concept of representative element volume (REV) [3], the fluid only flows through the pores formed by the solid matrix, instead of filling the whole porous medium. Although that procedure is in line with the objective physics, it generally brings huge computation load for tracking the fluid-solid interface, or in other word, the boundary treatment.

Pore-scale simulation by the traditional computational fluid dynamics that based on the Navier-Stokes (NS) equations, is usually considered to be a non-trivial task. On the other hand, the mesoscopic scheme of lattice Boltzmann equation (LBE) [4],[5] emerges as a competence. The LBE is derived from the Boltzmann equation where the distribution functions concerned evolve in the two steps of collision and streaming. The collision is completely localized. For the streaming, the distribution function originating from the interface is unknown and equals to the incoming counterpart; in addition, the interface can be reset artificially at the middle of a mesh. It is therefore this boundary treatment called the half-way (HW) bounce-back method [6]. Successful applications by the lattice Boltzmann method coupled with the HW bounce-back scheme have been extensively conducted in the literature [7–10]. The development of LBE over the past forty years has recently been reviewed comprehensively by He et al. [11].

At the same time, many variations of improved LBE have been developed [12–14]. Particularly, the DUGKS adopted in this study is recently proposed by Guo et al. [15], which solves the Boltzmann equation in a finite volume formulation, rather than the finite difference of LBE. The most distinguished feature of DUGKS lies in the use of discrete characteristic solutions of the Boltzmann equation to evaluate the micro-flux at the cell interface. That procedure contributes to a simple mathematical form for combining the effects of free migration and collision of the fictitious particles [41]. The temporal and spatial step sizes are not limited respectively by the mean collision time and the mean free path of particles in DUGKS. Despite relatively new, it has been implemented

* Corresponding author.
E-mail addresses: taoshi@dgut.edu.cn (S. Tao), heqing@dgut.edu.cn (Q. He).

https://doi.org/10.1016/j.compfluid.2020.104776
0045-7930/© 2020 Elsevier Ltd. All rights reserved.

in a variant of flow problems, from the continuum to free molecular regimes [16–18]. Note that the computational mesh is not so flexible in the LBE with a finite difference formulation [47]. Furthermore, it is a non-trivial task to simulate the non-continuum flows in the transition regime using LBE. Particularly, in the continuum regime, some comparative studies [20],[48],[49] have demonstrated that the DUGKS has some advantages of stability and accuracy over LBE.

Suitable boundary scheme should be specified in the simulations using DUGKS. The local bounce back method can be applied to handle the straight interface. For example, Wang et al. [19],[20] reported the plane channel flow blocked with a square cylinder, and thermal flow in a hollow cavity with strong convection. Some studies adopt the body-conformal mesh due to the finite volume formulation of the DUGKS, where the boundary condition can be conveniently incorporated in the computation. Zhu et al. [21] applied the DUGKS to high speed flow past two circular cylinders using unstructured meshes. Wang et al. [22] combined the arbitrary Lagrangian-Eulerian (ALE) approach with the DUGKS to simulate the low-speed continuum and rarefied flows with moving boundaries. It is noted that the generation of flexible meshes implemented for curved surface may be cumbersome with the increase of the number of solid bodies. On the other hand, since the solution of governing equations and the implementation of boundary condition is decoupled in the immersed boundary (IB) method [23], it is considered to be a promising approach for flows with complex geometry, and has recently been incorporated into the DUGKS for interface-resolved simulations of particle-laden flows [24]. The IB method is generally implemented within the Cartesian grid system, and hence the efforts for mesh generation can be removed. However, in the IB-DUGKS, the fluid-solid interface is discretized into a series of Lagrangian points, which serve as a generator of the external force added in the governing equations. Those terms should be evenly distributed to both sides of the boundary. As a result, the interface is smeared in several meshes. Such diffuse property may cause some unphysical phenomena in the simulations. For instance, the streamline may penetrate into the body interface, indicating a significant inconsistency between the computed and desired velocities [25],[26].

Another type of IB method is the sharp interface scheme, which includes the ghost-cell (GC) approach adopted in the present study. In the GC scheme [27–29], there is no need to introduce the body force into the governing equation. For the purpose to extend the flow solution to the solid domain, the solid cell that has at least one link intersected by the interface is transformed deliberately to be a fluid cell. The information at such cell is then extrapolated from the interface and the neighboring flow. The boundary condition at the interface is known in the simulation. Therefore, the key point to implement such extrapolation lies in the evaluation of the information at the image node, which is to be obtained by interpolation. Various kinds of interpolation schemes have been presented in the previous studies, such as the generalized bilinear interpolation [30] and constrained weighted least square [31]. Those high-order interpolation methods improve the accuracy at the cost of adding complexity with more neighboring nodes involved. That strategy hinders the applications of the GC method to the pore-scale simulation of porous media flows.

With the introduction of the HW-type method maturely used in LBE, the GC scheme can be dramatically simplified. The mainly objective of this paper is to promote the application of DUGKS for efficiently simulating the pore-scale porous media flows by the halfway ghost cell method. Two cases respectively with non-uniform mesh and rarefied flow effect are further conducted to demonstrate the versatility of the method. The remaining part of this paper is organized as follows. Section 2 is devoted to introduce a mathematical formulation of the present HWGC-DUGKS. The method is validated in Section 3. Finally, conclusions are drawn in Section 4.

2. Numerical method

2.1. Discrete unified gas kinetic scheme for low-speed flow

For continuum flows, the Knudsen number defined as $\mathrm{Kn} = \lambda/L$ is smaller than 0.001, where λ and L are the mean free path of the gas and the characteristic of the flow, respectively [15]. The incompressible viscous flow at the continuum regime can be subjected to the Navier-Stokes (NS) equations as

$$\nabla.\boldsymbol{u} = 0, \tag{1}$$

$$\frac{\partial \boldsymbol{u}}{\partial t} + \boldsymbol{u}.\nabla\boldsymbol{u} = -\frac{1}{\rho}\nabla p + \nu\nabla^2\boldsymbol{u} + \boldsymbol{a}_g, \tag{2}$$

where the $\boldsymbol{u}$, ρ, p and ν are the fluid velocity, density, pressure and viscosity. $\boldsymbol{a}_g$ is the external body force. For micro flows with rarefied effect, the NS equations may collapse at $\mathrm{Kn} > 0.1$ [15], but the Boltzmann equation still holds for such flows. Therefore, the Boltzmann equation is taken for consistency as the governing equation, which is expressed as [15]

$$\frac{\partial f}{\partial t} + \boldsymbol{\xi}.\nabla f = \frac{f^{eq} - f}{\tau} + F_g, \tag{3}$$

where f denotes the flow distribution function with velocity $\boldsymbol{\xi}$ at position $\boldsymbol{x}$ and time t. τ is the relaxation times in the Bhatnagar-Gross-Krook (BGK) collision operator. $f^{eq}$is the Maxwellian-type equilibrium distribution functions [30] as

$$f^{eq} = \frac{\rho}{2\pi RT}\exp\left(-\frac{(\boldsymbol{\xi} - \boldsymbol{u})^2}{2RT}\right). \tag{4}$$

R and T in Eq. (4) are the gas constant and temperature related to the artificial sound speed, respectively. F_g is the force term in the DUGKS [31] as

$$F_g = -\boldsymbol{a}_g.\nabla_\xi f \approx -\boldsymbol{a}_g.\nabla_\xi f^{eq} = \boldsymbol{a}_g.\frac{(\boldsymbol{\xi} - \boldsymbol{u})}{RT} f^{eq}, \tag{5}$$

For the conservative flow variables of ρ and $\boldsymbol{u}$, they are obtained from the moments of the distribution function, with the additional influence of the force as

$$\rho = \int f d\boldsymbol{\xi}, \quad \rho\boldsymbol{u} = \int \boldsymbol{\xi} f d\boldsymbol{\xi} + \frac{1}{2}\Delta t \rho \boldsymbol{a}_g. \tag{6}$$

2.1.1. Strang-Splitting scheme for body force

The external body force involved in the Eq. (3) should be first incorporate into the DUGKS. The Strang-Splitting algorithm [32] is used for such purpose in the present study. In that scheme, the force is divided into two equal parts, which respectively impact on the distribution function through the pre-forcing and post-forcing procedures as

$$\frac{\partial f}{\partial t} = \frac{1}{2}F_g, \tag{7}$$

$$\frac{\partial f}{\partial t} + \boldsymbol{\xi}.\nabla f = \Omega_f = \frac{f^{eq} - f}{\tau}, \tag{8}$$

$$\frac{\partial f}{\partial t} = \frac{1}{2}F_g. \tag{9}$$

Eq. (8) is the pure DUGKS process, which is to be introduced subsequently. As for the forcing steps given by Eqs. (7) and (9), both the distribution function and the macroscopic quantities should be updated as

$$f^* = f + 0.5\Delta t F_g, \tag{10}$$

$$\boldsymbol{u}^* = \boldsymbol{u} + 0.5\boldsymbol{a}_g\Delta t, \tag{11}$$

2.1.2. Discrete unified gas kinetic scheme

The DUGKS for the evolution of the fluid distribution function according to Eq. (8) is explained in this subsection. The temperature counterpart can be constructed similarly. The DUGKS applies the midpoint rule and the trapezoidal scheme respectively to the convection and collision terms and formulates a discrete time and space form of the Boltzmann Eq. (8) as [15],[33]

$$f_j^{n+1} - f_j^n + \frac{\Delta t}{|V_j|}F^{n+1/2} = \frac{\Delta t}{2}\left(\Omega_j^{n+1} + \Omega_j^n\right), \tag{12}$$

where V_j is the j-th control volume, Δt is the time step, and

$$F^{n+1/2} = \int_{\partial V_j}\left(\boldsymbol{\xi}.\boldsymbol{n}\right)f(\boldsymbol{x}, t_{n+1/2})d\boldsymbol{S}, \tag{13}$$

is the microscopic flux across the cell interface with the outward unit vector normal $\boldsymbol{n}$. Here, the $f_j^n$and $\Omega_j^n$are the volume-averaged values in cell V_j, which has a volume of $|V_j|$ and surface ∂V_j. Note that $f_j$cannot be explicitly updated through the Eq. (12) due to the existence of collision term Ω_j^{n+1}. Two new distribution functions are introduced for eliminating such implicity,

$$\widetilde{f} = f - \frac{\Delta t}{2}\Omega, \ . \ \widetilde{f}^+ = f + \frac{\Delta t}{2}\Omega. \tag{14}$$

Eq. (12) can then be rewritten as

$$\widetilde{f}_j^{n+1} = \widetilde{f}_j^{+,n} - \frac{\Delta t}{|V_j|}F^{n+1/2}. \tag{15}$$

Note that the following relationship holds between those two auxiliary distribution functions as

$$\widetilde{f}^+ = \frac{2\tau - \Delta t}{2\tau + \Delta t}\widetilde{f} + \frac{2\Delta t}{2\tau + \Delta t}f^{eq}. \tag{16}$$

In addition, with the fact that the moments of the collision term equal to zero, the conserved variables can be directly obtained from $\tilde{f}$according to the Eq. (6), and hence the $\tilde{f}$is actually updated in the simulations.

The remaining task is to identify the flux $F^{n+1/2}$for updating the $\tilde{f}$, where the distribution function at the cell interface and time $(t_n + \Delta t/2)$ should be evaluated. For such purpose, we integrate the Boltzmann Eq. (8)along the characteristic line with a time step $h = \Delta t/2$,

$$\begin{aligned} &f(\boldsymbol{x}_b, \boldsymbol{\xi}, t_n + h) - f(\boldsymbol{x}_b - \boldsymbol{\xi}h, \boldsymbol{\xi}, t_n) \\ &= \frac{h}{2}\left[\Omega(\boldsymbol{x}_b, \boldsymbol{\xi}, t_n + h) + \Omega(\boldsymbol{x}_b - \boldsymbol{\xi}h, \boldsymbol{\xi}, t_n)\right], \end{aligned} \tag{17}$$

where $\boldsymbol{x}_b$ is a node at the cell interface, and the trapezoidal rule is again applied to the collision operator. Another two auxiliary distribution functions are introduced to make Eq. (17) explicit,

$$\overline{f} = f - \frac{h}{2}\Omega, \quad \overline{f}^+ = f + \frac{h}{2}\Omega, \tag{18}$$

with

$$\overline{f}^+ = \frac{2\tau - h}{2\tau + h}\overline{f} + \frac{2h}{2\tau + h}f^{eq}. \tag{19}$$

Then we can obtain

$$\overline{f}(\boldsymbol{x}_b, \boldsymbol{\xi}, t_n + h) = \overline{f}^+(\boldsymbol{x}_b - \boldsymbol{\xi}h, \boldsymbol{\xi}, t_n). \tag{20}$$

The distribution function on the right hand side of Eq. (20) can be reconstructed as

$$\overline{f}(\boldsymbol{x}_b, \boldsymbol{\xi}, t_n + h) = \overline{f}^+(\boldsymbol{x}_b, \boldsymbol{\xi}, t_n) - \boldsymbol{\xi}h.\nabla\overline{f}^+(\boldsymbol{x}_b, \boldsymbol{\xi}, t_n). \tag{21}$$

With the Eq. (23) at hand, the distribution function at the cell interface at time $t_n + h$ can be obtained,

$$\begin{aligned} f(\boldsymbol{x}_b, \boldsymbol{\xi}, t_n + h) = &\frac{2\tau}{2\tau + h}\overline{f}(\boldsymbol{x}_b, \boldsymbol{\xi}, t_n + h) \\ &+ \frac{h}{2\tau + h}f^{eq}(\boldsymbol{x}_b, \boldsymbol{\xi}, t_n + h), \end{aligned} \tag{22}$$

where the macroscopic quantities is evaluated from $\tilde{f}(\boldsymbol{x}_b, \boldsymbol{\xi}, t_n + h)$according to Eq. (6). Finally, the flux $F^{n+1/2}$ is then computed by Eq. (13), and the evolution of $\tilde{f}$ can be processed according to Eq. (15). It is noted that the following two relations will be used in the computation,

$$\overline{f}^+ = \frac{2\tau - h}{2\tau + \Delta t}\widetilde{f} + \frac{3h}{2\tau + t}f^{eq}, \tag{23}$$

$$\widetilde{f}^+ = \frac{4}{3}\overline{f}^+ - \frac{1}{3}\widetilde{f} \tag{24}$$

The temporal and spatial discretization of the BGK-type Boltzmann Eq. (8) is completed by now. As a discrete ordinate method, the only remaining task in DUGKS is to discretize the velocity space. For continuum flows, the three-point Gauss-Hermite quadrature and the tensor product method [15],[34] are adopted in this study to obtain a minimum set of the discrete particle velocities and corresponding weights for one and higher dimension problems. The following nine velocity model will be applied for the 2D continuum flows considered in the present study,

$$\boldsymbol{\xi}_i = \begin{cases} (0,0), & i = 0, \\ (\pm 1, 0)c, \ (0, \pm 1)c, & i = 1 - 4, \\ (\pm 1, \pm 1)c, & i = 5 - 8, \end{cases} \tag{25}$$

where $c = \sqrt{3RT}$ is the model speed of sound. The associated weights are $W_0 = 4/9$, $W_{1,2,3,4} = 1/9$, $W_{5,6,7,8} = 1/36$. For non-continuum flows, the non-equilibrium effect emerges and more discrete velocities are indispensable in the simulation. Therefore, the 28 points half range Gauss-Hermite quadrature rule is used to identify the discrete velocities $\boldsymbol{\xi}_i$and weight**s** W_0 [33]. Under the assumption of low Mach number that satisfies $Ma = |\boldsymbol{u}|/c_s = |\boldsymbol{u}|/\sqrt{RT} \ll 1.0$, a discrete equilibrium distribution function which includes the second-order term of Macan be

$$f_i^{eq} = W_i\rho\left[1 + \frac{\boldsymbol{\xi}_i.\boldsymbol{u}}{RT} + \frac{\left(\boldsymbol{\xi}_i.\boldsymbol{u}\right)^2}{2(RT)^2} - \frac{|\boldsymbol{u}|^2}{2RT}\right]. \tag{26}$$

The macroscopic quantities, i.e., ρ, $\boldsymbol{u}$, p and ν are evaluated as

$$\rho = \sum_i f_i, \quad \rho\boldsymbol{u} = \sum_i \boldsymbol{\xi}_i f_i, \quad p = \rho RT, \quad \nu = \tau RT. \tag{27}$$

2.2. Half-way ghost-cell method for curved interface

It is a non-trivial task to handle the curved boundaries within the Cartesian mesh in the DUGKS. The ghost-cell (GC) approach is applied for such purpose in this study, where the first procedure is to classify the status of the cells. A general configuration is delineated in Fig. 1. The fluid and solid cells are the center of the computational meshes located at the fluid and solid domains, respectively. The solid cell which center has at least one link intersected by the interface are further transformed to be the ghost cell. The information at that cell is unknown, which is to be evaluated from the interface and the neighboring flow. The half-way (HW) approach is further introduced here to remove the difficulty to identify the location of the real interface, where it is always set at the middle of the mesh.

Taking point G in Fig. 1 for example, it is the center of a ghost cell, and (I_1, I_2) and (F_1, F_2) are the corresponding intersection and fluid nodes. It is obvious that the intersection points overlap with the interface centers. The distribution function $\tilde{f}$at G is concerned

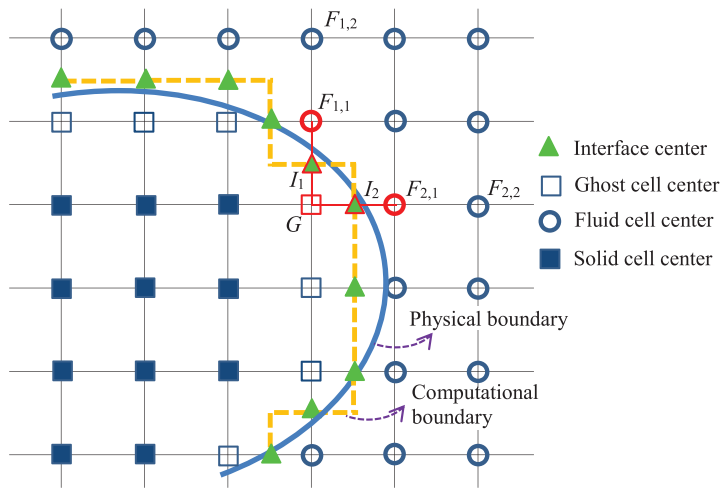

Fig. 1. Schematic of the half-way ghost-cell method. Point G is the center of a ghost cell, which is in the solid domain and has at least one link intersected by the fluid-solid interface (physical boundary). The corresponding intersection points, i.e., I_1 and I_2 are artificially reset at the middle of the mesh, and hence overlap with the interface center. $F_{1,1}$ and $F_{2,1}$ are the neighboring fluid cell centers, which is in mirror symmetry with G regarding to the interface. $F_{1,2}$ and $F_{2,2}$ are two further fluid cell centers along the grids. As a result, the interface is approximated as zig-zag lines (computational boundary).

in the boundary treatment. For continuum flows, it is decomposed into the equilibrium and non-equilibrium parts [46] as

$$\widetilde{f}\left(\boldsymbol{x}_G, \boldsymbol{\xi}_i, t\right) = f^{eq}\left(\boldsymbol{x}_G, \boldsymbol{\xi}_i, t\right) + f^{neq}\left(\boldsymbol{x}_G, \boldsymbol{\xi}_i, t\right), \tag{28}$$

According to the Eq. (26), the equilibrium part is directly obtained from the macroscopic quantities of the density and velocity as $f^{eq}(\boldsymbol{x}_G) = f^{eq}(\rho(\boldsymbol{x}_G), \boldsymbol{u}(\boldsymbol{x}_G))$. As outlined previously, $\rho(\boldsymbol{x}_G)$, $\boldsymbol{u}(\boldsymbol{x}_G)$and $f^{neq}(\boldsymbol{x}_G)$are to be extrapolated from the interface and the neighboring flow. There are two kinds of boundary treatment for those quantities involved in the present study, i.e., the Dirichlet and the Neumann conditions. The velocity is subjected to the Dirichlet condition, where its value is known constant at the intersection node. Therefore, a linear extrapolation can be applied as

$$\boldsymbol{u}(\boldsymbol{x}_G) = \frac{1}{N}\sum_{n=1}^{N}\left(2\boldsymbol{u}(\boldsymbol{x}_{I_n}) - \boldsymbol{u}(\boldsymbol{x}_{F_{n,1}})\right). \tag{29}$$

Note that the extrapolated velocity is averaged by the total directions ($N = 2$ for point G in the Fig. 1) in the above Eq. (29). The density is generally assumed to subject to the Neumann condition with zero normal gradient [28],[35],[36], i.e., $\rho(\boldsymbol{x}_W)/\boldsymbol{n} = 0$, which has

$$\rho(\boldsymbol{x}_G) = \frac{1}{N}\sum_{n=1}^{N}\left(\rho(\boldsymbol{x}_{I_n}) - \frac{\partial\rho(\boldsymbol{x}_{I_n})}{\partial\boldsymbol{n}}\Delta x\right) = \frac{1}{N}\sum_{n=1}^{N}\rho(\boldsymbol{x}_{I_n}). \tag{30}$$

The non-equilibrium part can be determined analogically with $f^{neq}(\boldsymbol{x}_I)/\boldsymbol{n} = 0$,

$$f^{neq}(\boldsymbol{x}_G) = \frac{1}{N}\sum_{n=1}^{N} f^{neq}(\boldsymbol{x}_{I_n}). \tag{31}$$

After the evaluation of the density, velocity and the non-equilibrium distribution function, the distribution functions can be evaluated according to the Eq. (28) at the continuum flows.

For non-continuum flows, the gas velocity at the wall surface is unknown because of the existence of the slip velocity, and the conditions for the density and the non-equilibrium distribution function are both undetermined. Therefore, the construction of the distribution function at the ghost cell center is different from the continuum counterparts. At this time, some distribution functions at the interface center are first extrapolated from the neighboring fluid cells as

$$\widetilde{f}\left(\boldsymbol{x}_{I_n}, \boldsymbol{\xi}_i, t\right) = 1.5\widetilde{f}\left(\boldsymbol{x}_{F_{n,1}}, \boldsymbol{\xi}_i, t\right) - 0.5\widetilde{f}\left(\boldsymbol{x}_{F_{n,2}}, \boldsymbol{\xi}_i, t\right), \qquad \boldsymbol{\xi}_i.\boldsymbol{n} < 0. \tag{32}$$

Note that the Eq. (32) is for the distribution functions with velocity pointing to the solid zone. As for the distribution functions reflecting from the wall, they are evaluated by the Maxwellian diffuse-scattering rule as

$$\widetilde{f}\left(\boldsymbol{x}_{I_n}, \boldsymbol{\xi}_i, t\right) = f^{eq}(\rho_w, \boldsymbol{u}_w), \qquad \boldsymbol{\xi}_i.\boldsymbol{n} > 0. \tag{33}$$

The wall density in the Eq. (33) is unknown, and is to be identified by the non-penetration condition,

$$\sum_{\boldsymbol{\xi}_i.\boldsymbol{n}<0}\left(\boldsymbol{\xi}_i.\boldsymbol{n}\right)\widetilde{f}\left(\boldsymbol{x}_{I_n}, \boldsymbol{\xi}_i, t\right) + \sum_{\boldsymbol{\xi}_i.\boldsymbol{n}>0}\left(\boldsymbol{\xi}_i.\boldsymbol{n}\right)f^{eq}(\rho_w, \boldsymbol{u}_w) = 0. \tag{34}$$

Combined with the Eq. (26), the density can be expressed succinctly as

$$\rho_w = -\frac{\sum_{\boldsymbol{\xi}_i.\boldsymbol{n}<0}\left(\boldsymbol{\xi}_i.\boldsymbol{n}\right)\widetilde{f}\left(\boldsymbol{x}_{I_n}, \boldsymbol{\xi}_i, t\right)}{\sum_{\boldsymbol{\xi}_i.\boldsymbol{n}>0}\left(\boldsymbol{\xi}_i.\boldsymbol{n}\right)f^{eq}(1, \boldsymbol{u}_w)}. \tag{35}$$

The distribution functions in the non-continuum regime can then be obtained by extrapolation from the points I_n and $F_{n,1}$ as

$$\widetilde{f}\left(\boldsymbol{x}_G, \boldsymbol{\xi}_i, t\right) = \frac{1}{N}\sum_{n=1}^{N}\left[2\widetilde{f}\left(\boldsymbol{x}_{I_n}, \boldsymbol{\xi}_i, t\right) - \widetilde{f}\left(\boldsymbol{x}_{F_{n,1}}, \boldsymbol{\xi}_i, t\right)\right], \ . \tag{36}$$

3. Results and discussion

In this section, the accuracy and feasibility of the present HWGC-DUGKS is to be tested through the pore-scale simulation of porous media flows, including the cylindrical Couette flow, flow through a square array of cylinders and flow in the random porous media. It is noted that simulations in this study are all performed in the incompressible flow limit (Mach number $Ma = 0.1$) with $RT = 1/3$. The time step is determined by the Courant-Friedrichs-Lewy (CFL) number in DUGKS as

$$\Delta t = CFL\left(\frac{\Delta x}{|\boldsymbol{\xi}_i|}\right)_{\min}, \tag{37}$$

where Δx is the spatial step, and CFL is set to be 0.8.

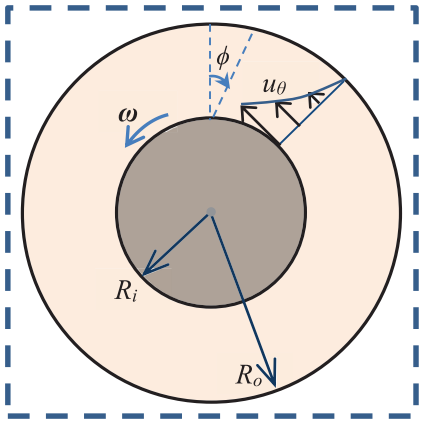

Fig. 2. Schematic of the cylindrical Couette flow. The dash line denotes the computational domain.

3.1. Cylindrical Couette flow

The accuracy of the present HWGC-DUGKS is first explored in the cylindrical Couette flow. It is a classic fluid dynamics problem involving relatively complex geometries. The flow arrangement is illustrated in Fig. 2. As can be seen, the fluid is confined by two concentric cylinders with radii R_i and R_o, respectively. The outer cylinder is stationary, and the inner one rotates with speed ω_i. At steady state, analytical solution of the velocity can be obtained for this flow as [37]

$$u_\theta = \frac{\left(R_i^2 R_o^2 - R_i^2 r^2\right)\omega_i}{\left(R_o^2 - R_i^2\right) r}, \quad u_r = 0, \tag{38}$$

where u_θ, u_r are the velocity components, and r is the radial distance. The flow Reynolds number Re is defined as $\omega_i R_i (R_o - R_i)/\nu$, with $R_o = 2R_i$ considered in this study. Since the ghost point of the outer interface locates outside the cylinder, the computational domain should be set to have several more grids than the diameter of the outer cylinder. The numerical error is evaluated as

$$E_2 = \sqrt{\sum\left[\left(u_{\theta,p} - u_\theta\right)^2 + \left(u_{r,p} - u_r\right)^2\right] / \sum\left(u_\theta^2 + u_r^2\right)}, \tag{39}$$

where the $u_{\theta,p}$ and $u_{r,p}$ are the velocity components obtained by the present HWGC-DUGKS, and the summation is over all the fluid points in the annulus.

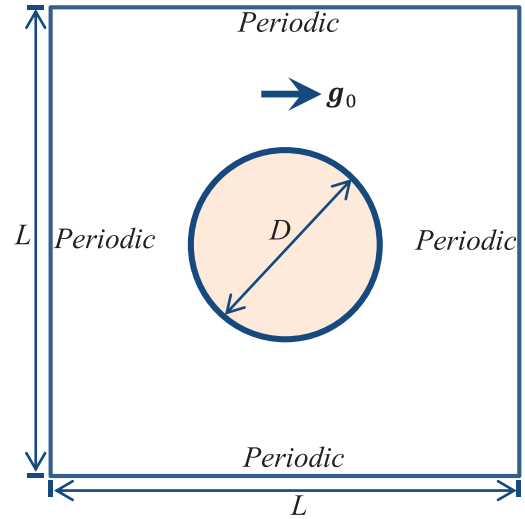

Fig. 4. Schematic of the flow through a square array of cylinders.

The velocity profile at $\phi = 0$ is presented in Fig. 3(a), where the characteristic length is resolved by a relatively small grid resolution of 10 meshes. τ equals to Δt and is fixed at $0.8/\sqrt{2}$. It can be observed that the results obtained by the present HWGC-DUGKS are in good agreement with those of the analytical data given by Eq. (38). Furthermore, Fig. 3(b) depicts the numerical error at different grid resolutions with $Re = 10$. The convergence rate indicates the present method is generally first-order accurate in space.

3.2. Flow through square array of circular cylinders

Simulation of flow through a square array of circular cylinders is further performed to validate the present HWGC-DUGKS. The flow condition is illustrated in Fig. 4. A circular cylinder with diameter D is concentrically embedded in the square computational domain with side length $L = 2D$. In order to model the flow in the porous media, periodic conditions are specified at all the outer boundaries. The fluid is driven from left to right by a constant external force $g_0 = 1.0 \times 10^{-8}$. A uniform mesh system of 100×100 is first applied in the simulations. As depicted in Fig. 5, the same problem is also investigated using a non-uniform mesh of 82×82, where the minimum and maximum spatial steps are $\Delta x_{min} = 1$ and $\Delta x_{max} = 10$, respectively. The permeability K of porous media

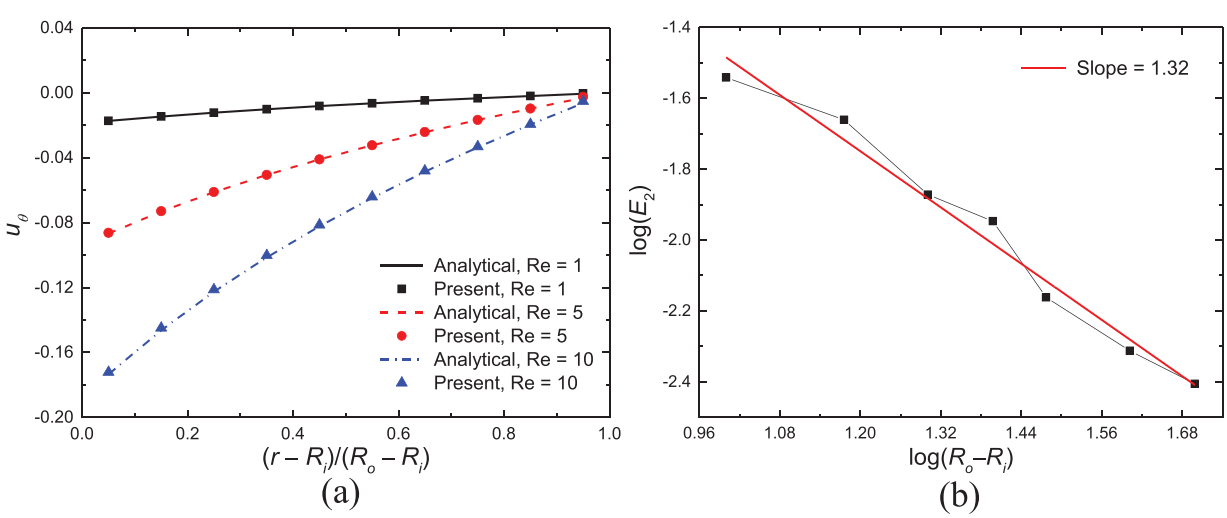

Fig. 3. Velocity profiles between the two concentric cylinders at $\phi = 0$ (a) and the relative errors under different grid resolutions at $Re = 10$ (b).

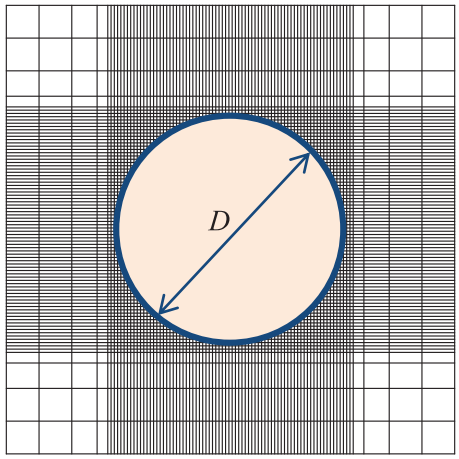

Fig. 5. The non-uniform mesh of 82 × 82 used in the simulation.

is the parameter concerned for this flow problem. At small *Re*, it is expressed by the Darcy's law as

$$K = -\frac{\rho \nu U}{g_0}, \tag{40}$$

where U is the apparent velocity of porous media, obtained by averaging the velocities within the whole computational domain. Theoretical solution of the permeability given by Sangani and Acrivos [38] is written as

$$K_a = \frac{D^2}{32\phi}\left(-\ln\phi - 1.476 + 2\phi - 1.774\phi^2 + 4.706\phi^3\right), \tag{41}$$

where the solid volume fraction ϕ equals to $0.25\pi D^2/L^2$. It is worth noting that there are some other analytical solutions available in the literature as reviewed by Chai et al. [39].

The streamlines and velocity contour around the cylinder at uniform and non-uniform meshes with $\tau = \Delta t$ are exhibited in Fig. 6. As can be observed, the flow is symmetric about the horizontal centerline of the cylinder. The fluid achieves a higher velocity when moving through the throat channel formed by two adjacent cylinders. Table 1 further presents the relative error of the permeability by the present HWGC-DUGKS, where the theoretical solution of Eq. (41) is taken as reference. Reasonable agreements can be always obtained at different relaxation times. Moreover, the relative error of the permeability reduces for all the non-uniform cases, with less computing times. Note that it is a non-trivial task to use flexible mesh in the LBE [45].

Table 1
The relative error of the permeability by the HWGC-DUGKS at different τ with uniform mesh of 100 × 100 and non-uniform mesh of 82 × 82.

Relative Error	$\tau = 0.5\Delta t$	$\tau = \Delta t$	$\tau = 1.5\Delta t$	$\tau = 2\Delta t$
Uniform mesh	−3.8%	−3.1%	−2.6%	−2.0%
Non-uniform mesh	−1.90%	−1.16%	0.64%	−0.16%

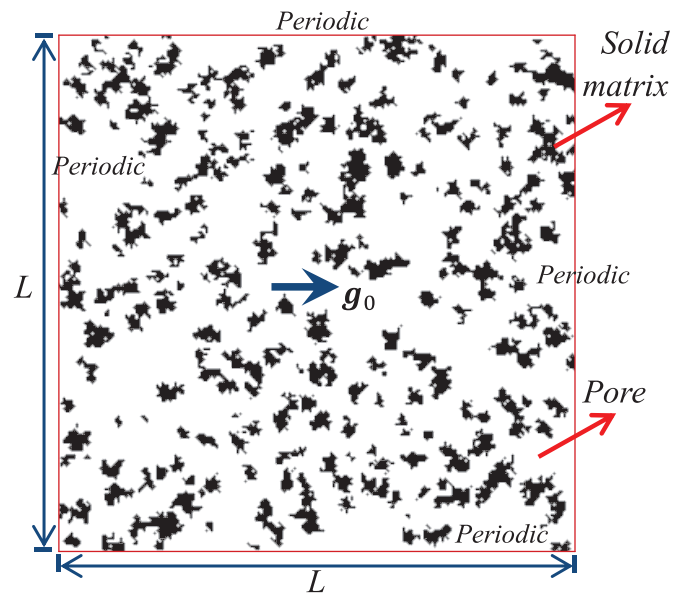

Fig. 7. Schematic of the random porous media produced by the QSGS method.

3.3. Flow through random porous media

The flow through the random porous media is considered in this subsection. The flow is more complex compared with the ordered porous media flow. To accomplish the simulation, the first procedure is to construct the random porous structure. The quartet structure generation set (QSGS) method proposed by Wang et al.

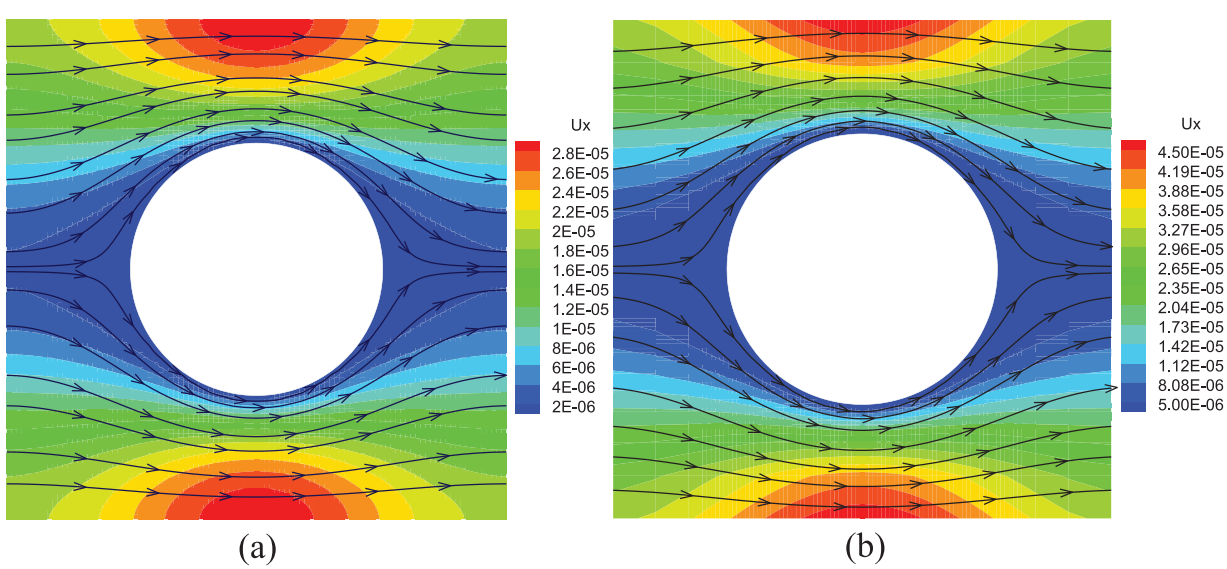

Fig. 6. The streamlines and contour of streamwise velocity around the cylinder with uniform (a) and non-uniform (b) meshes at $\tau = \Delta t$.

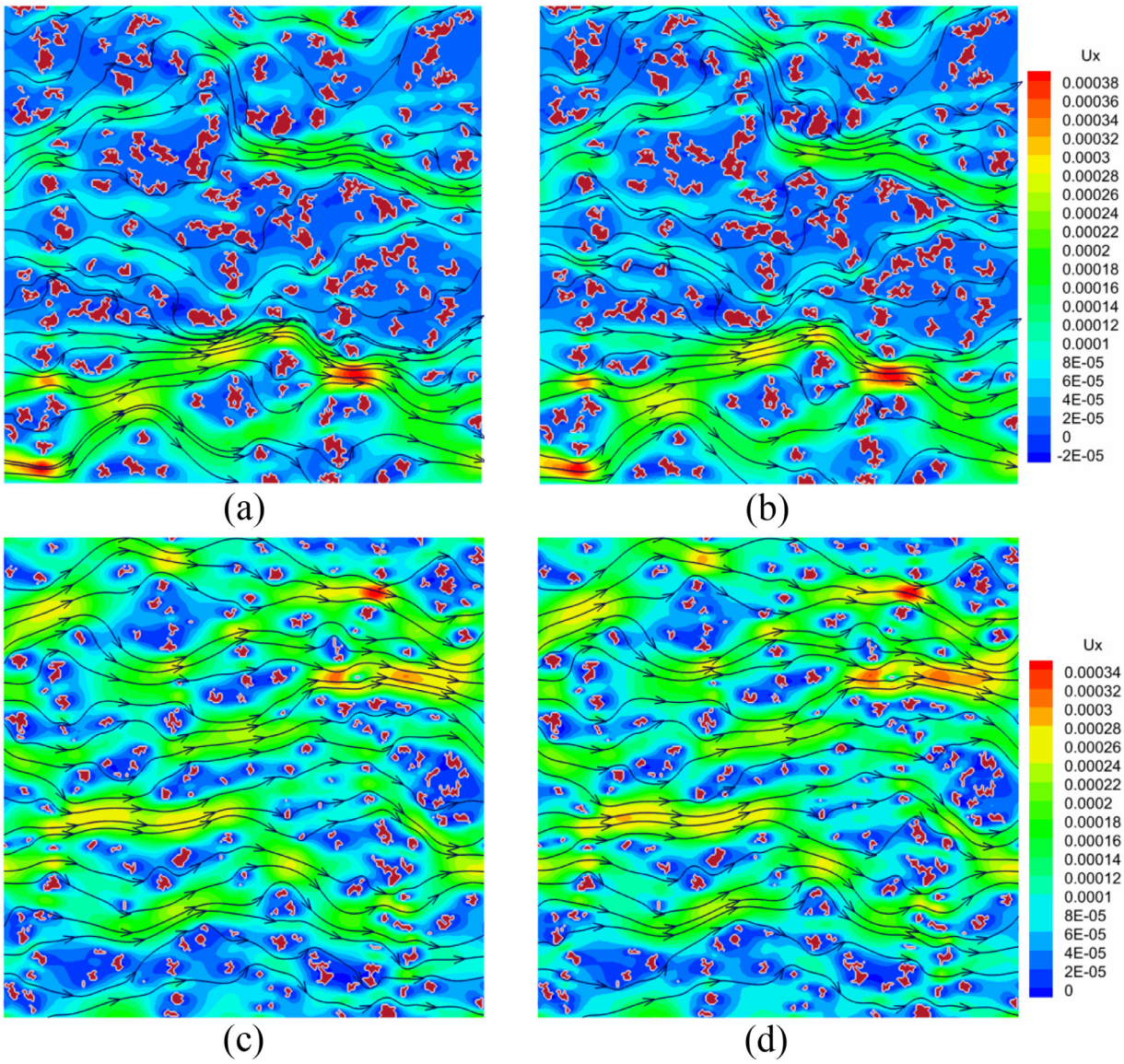

Fig. 8. Flow through the random porous media at the porosities $\varepsilon = 0.9$ (a,b) and 0.95 (c,d) using the LBE (a,c) and present HWGC-DUGKS (b,d).

[40] is adopted for such purpose in this study. In the QSGS, some seeds are randomly distributed in the computational domain at the beginning, and the solid matrix then starts to grow on the base of those seeds. The random porous media produced by the QSGS is depicted in Fig. 7. The flow is driven by a constant horizontal force $g_0 = 1.0 \times 10^{-6}$, which is small enough to render a Stokes flow in the porous media. The periodic condition is applied to the outer boundaries. A mesh system of 200×200 is used in the simulations. The kinematic viscosity ν is fixed at 1/3.

The streamlines and the velocity contour in the x-direction are presented in Fig. 8. The results obtained by the lattice Boltzmann equation (LBE) with the same computation condition is also included for comparison. It can be observed that the flow meanders through the random porous media. And the flow image obtained by the HWGC-DUGKS is consistent with that of LBE. The permeability computed according to the Eq. (40) is listed in Table 2. The present results again agree well with those of the LBE.

Table 2
Comparison of the permeability by the LBE and the HWGC-DUGKS.

K/L^2	$\varepsilon = 0.9$	$\varepsilon = 0.95$
LBM	2.72×10^{-4}	4.26×10^{-4}
HWGC-DUGKS	2.81×10^{-4}	4.40×10^{-4}
Relative error	3.7%	3.3%

3.4. Micro flow in ordered porous media

The micro flow past a square array of circular cylinders is simulated in this subsection to further demonstrate the versatility of the present method. The flow configuration is analogous to that depicted in Fig. 4, except for the inclusion of the rarefied effect here. This problem has been extensively studied by the numerical methods of NS equations with the slip boundary condition [42], direct simulation Monte Carlo (DSMC) [43], discrete velocity model (DVM) [43] and unified gas kinetic scheme (UGKS) [44].

In the micro flows, the control parameter is the Kn number and is used to evaluate the relaxation time,

$$\tau = KnL\sqrt{\frac{2}{\pi RT}}, \tag{42}$$

which is derived from the relationship between τ and λ as $\lambda = \mu\sqrt{\pi RT/2}/p = \tau\sqrt{\pi RT/2}$ [15]. The numerical parameters are the

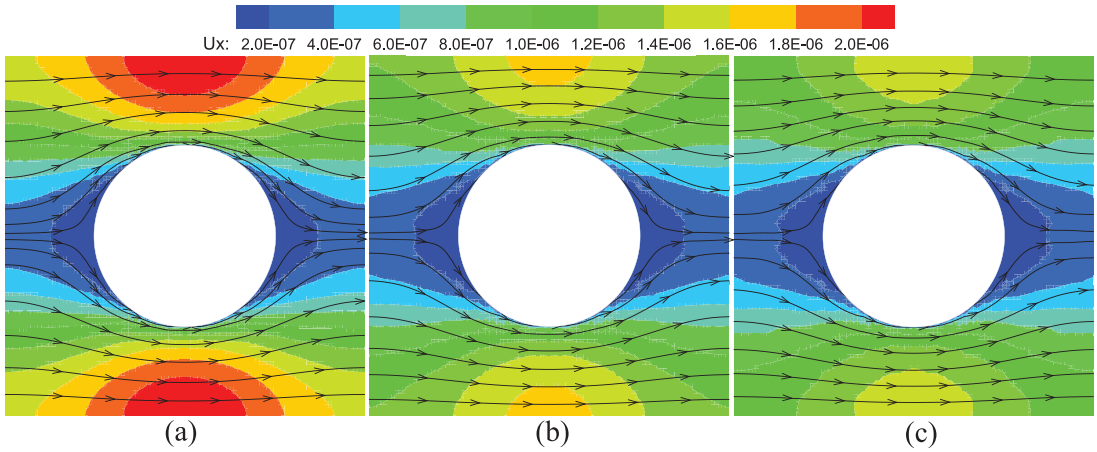

Fig. 9. The streamlines and contour of streamwise velocity around the cylinder at Kn = 0.1 (a), 0.2 (b) and 0.3 (c).

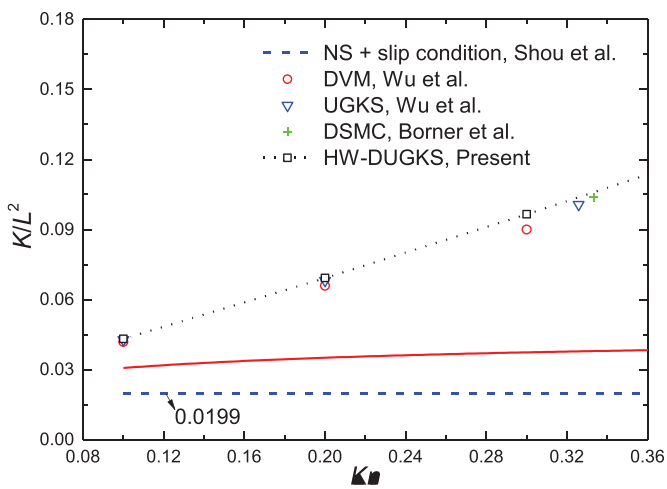

Fig. 10. The dimensionless permeability at different Kn numbers with $\varepsilon = 0.8$. The dash line with constant value of 0.0199 is the no-slip permeability at Kn = 0 according to the Eq. (41).

same with that of the above mentioned case of continuum flow with uniform mesh. The discrete velocities $\boldsymbol{\xi}_i$ and weights W_0 are obtained by the 28 points half range Gauss-Hermite quadrature rule [33]. Furthermore, the Maxwellian diffuse-scattering boundary condition exerted on the wall surface is implemented by the present HWGC-GUDKS. Three sets of Kn = 0.1, 0.2 and 0.3 are considered in the simulation. The porosity is fixed at $\varepsilon = 0.8$. The other numerical parameters are the same with those of the above-mentioned continuum flow case with uniform mesh of 100 × 100.

The streamlines and contour of streamwise velocity are illustrated in Fig. 9. It can be observed that the velocity reduces with the increase of the Kn, due to the larger viscosity. Fig. 10 exhibits the permeability normalized by L^2. The rarefied effect facilitates an obvious growth of the permeability. Furthermore, the results by the NS equations combined with the slip boundary condition [42] deviate from the those by the kinetic methods at Kn > 0.1, indicating a collapse of the method at this time. The numerical results by the other method are generally in consistency.

4. Conclusions

In this study, a half-way ghost-cell discrete unified gas kinetic scheme (HWGC-DUGKS) is developed for the pore-scale simulation of porous media flows. The external force is conveniently incorporated into the DUGKS by the Strang-Splitting method. The ghost cell approach is combined for handling the hydrodynamic boundary condition at the fluid-solid interface. Particularly, with the introduction of the half-way-type approach, the interface is assumed to be located at the middle of a mesh, and then the implementation of the ghost-cell approach can be dramatically simplified. Simulations of the cylindrical Couette flow, flow through a square array of cylinders and flow in the random porous media are performed to validate the present HWGC-DUGKS. Particularly, the non-uniform mesh and rarefied effect are considered in the ordered porous media flows. The results demonstrate the accuracy and feasibility of the method for pore-scale porous media flows.

Declaration of Competing Interest

The authors declare that there is no conflict of interest.

CRediT authorship contribution statement

Shi Tao: Conceptualization, Methodology, Software, Writing - review & editing. **Liang Wang:** Data curation, Writing - original draft. **Ya Ge:** Visualization, Investigation. **Qing He:** Supervision.

Acknowledgments

Shi Tao is very much thankful to Profs. Zhaoli Guo, Dr. Lianhua Zhu and Dr. Chuang Zhang for insightful discussions. This work was supported by the National Natural Science Foundation of China (51906044, 51776068 and 11902075) the Doctoral Start-up Foundation of Dongguan University of Technology, China (Grant No. GC300502–39), the Guangdong Provincial Key Laboratory of Distributed Energy Systems, China (2020B1212060075), and the Guangdong Provincial Key Platforms and Major Scientific Research Projects in Colleges and Universities, Featured Innovation Program (Grant No. 2018KTSCX225).

Supplementary materials

Supplementary material associated with this article can be found, in the online version, at doi:10.1016/j.compfluid.2020.104776.

References

[1] Parvan A, Jafari S, Rahnama M, Raoof A. Insight into particle retention and clogging in porous media; a pore scale study using lattice Boltzmann method. Adv Water Resour 2020;138:103530.

[2] Zhang C, Suekane T, Minokawa K, Hu Y, Patmonoaji A. Solute transport in porous media studied by lattice Boltzmann simulations at pore scale and x-ray tomography experiments. Phys Rev E 2019;100(6):063110.
[3] Zhao T, Zhao H, Ning Z, Li X, Wang Q. Permeability prediction of numerical reconstructed multiscale tight porous media using the representative elementary volume scale lattice Boltzmann method. Int J Heat Mass Transf 2018;118:368–77.
[4] Aidun CK, Clausen JR. Lattice-Boltzmann method for complex flows. Annu Rev Fluid Mech 2010;42:439–72.
[5] Guo Z, Shu C. Lattice boltzmann method and its applications in engineering, Vol. 3. World Scientific; 2013.
[6] Ladd AJ. Lattice-Boltzmann methods for suspensions of solid particles. Mol Phys 2015;113(17–18):2531–7.
[7] Chai Z, Huang C, Shi B, Guo Z. A comparative study on the lattice Boltzmann models for predicting effective diffusivity of porous media. Int J Heat Mass Transf 2016;98:687–96.
[8] Ginzburg I, Silva G, Talon L. Analysis and improvement of Brinkman lattice Boltzmann schemes: bulk, boundary, interface. Similarity and distinctness with finite elements in heterogeneous porous media. Physical Review E 2015;91(2):023307.
[9] Maier RS, Bernard RS. Lattice-Boltzmann accuracy in pore-scale flow simulation. J Comput Phys 2010;229(2):233–55.
[10] Tao S, Guo Z. Boundary condition for lattice Boltzmann modeling of microscale gas flows with curved walls in the slip regime. Physical Review E 2015;91(4):043305.
[11] He YL, Liu Q, Li Q, Tao WQ. Lattice Boltzmann methods for single-phase and solid-liquid phase-change heat transfer in porous media: a review. Int J Heat Mass Transf 2019;129:160–97.
[12] Saadat MH, Bösch F, Karlin IV. Semi-Lagrangian lattice Boltzmann model for compressible flows on unstructured meshes. Physical Review E 2020;101(2):023311.
[13] Rao PR, Schaefer LA. Numerical stability of explicit off-lattice Boltzmann schemes: a comparative study. J Comput Phys 2015;285:251–64.
[14] Shu C, Wang Y, Teo CJ, Wu J. Development of lattice Boltzmann flux solver for simulation of incompressible flows. Adv Appl Math Mech 2014;6(4):436–60.
[15] Guo Z, Xu K, Wang R. Discrete unified gas kinetic scheme for all Knudsen number flows: low-speed isothermal case. Physical Review E 2013;88(3):033305.
[16] Li C, Wang LP. An immersed boundary-discrete unified gas kinetic scheme for simulating natural convection involving curved surfaces. Int J Heat Mass Transf 2018;126:1059–70.
[17] Huo Y, Rao Z. The discrete unified gas kinetic scheme for solid-liquid phase change problem. Int Comm Heat and Mass Transf 2018;91:187–95.
[18] Tao S, He Q, Wang L, Huang S, Chen B. A non-iterative direct-forcing immersed boundary method for thermal discrete unified gas kinetic scheme with Dirichlet boundary conditions. Int J Heat Mass Transf 2019;137:476–88.
[19] Wang P, Zhang Y, Guo Z. Numerical study of three-dimensional natural convection in a cubical cavity at high Rayleigh numbers. Int J Heat Mass Transf 2017;113:217–28.
[20] Wang P, Zhu L, Guo Z, Xu K. A comparative study of LBE and DUGKS methods for nearly incompressible flows. Commun Comput Phys 2015;17(3):657–81.
[21] Zhu L, Guo Z, Xu K. Discrete unified gas kinetic scheme on unstructured meshes. Comput Fluids 2016;127:211–25.
[22] Wang Y, Zhong C, Liu S. Arbitrary Lagrangian-Eulerian-type discrete unified gas kinetic scheme for low-speed continuum and rarefied flow simulations with moving boundaries. Physical Review E 2019;100(6):063310.
[23] Tao S, Zhang HL, Guo ZL, Wang LP. A combined immersed boundary and discrete unified gas kinetic scheme for particle-fluid flows. J Comput Phys 2018;375(15):498–518.
[24] Peskin CS. The immersed boundary method. Acta numerica 2002;11:479–517.
[25] Seta T, Hayashi K, Tomiyama A. Analytical and numerical studies of the boundary slip in the immersed boundary-thermal lattice Boltzmann method. Int J Numer Methods Fluids 2018;86(7):454–90.
[26] Tao S, He Q, Chen J, Chen B, Yang G, Wu Z. A non-iterative immersed boundary-lattice Boltzmann method with boundary condition enforced for fluid—solid flows. Appl Math Model 2019;76:362–79.
[27] Tseng YH, Ferziger JH. A ghost-cell immersed boundary method for flow in complex geometry. J Comput Phys 2003;192(2):593–623.
[28] Tiwari A, Vanka SP. A ghost fluid Lattice Boltzmann method for complex geometries. Int J Numer Methods Fluids 2012;69(2):481–98.
[29] Chen S, Xu K, Li Z. Cartesian grid method for gas kinetic scheme on irregular geometries. J Comput Phys 2016;326:862–77.
[30] Shang J, Chai Z, Wang H, Shi B. Discrete unified gas kinetic scheme for nonlinear convection-diffusion equations. Physical Review E 2020;101(2):023306.
[31] Wu C, Shi B, Chai Z, Wang P. Discrete unified gas kinetic scheme with a force term for incompressible fluid flows. Computers & Mathematics with Applications 2016;71(12):2608–29.
[32] Dellar PJ. An interpretation and derivation of the lattice Boltzmann method using Strang splitting. Computers & Mathematics with Applications 2013;65(2):129–41.
[33] Guo Z, Wang R, Xu K. Discrete unified gas kinetic scheme for all Knudsen number flows. II. Thermal compressible case. Physical Review E 2015;91(3):033313.
[34] Yang LM, Shu C, Wu J, Wang Y. Comparative study of discrete velocity method and high-order lattice Boltzmann method for simulation of rarefied flows. Comput Fluids 2017;146:125–42.
[35] Huo Y, Rao Z. The numerical investigation of nanofluid based cylinder battery thermal management using lattice Boltzmann method. Int J Heat Mass Transf 2015;91:374–84.
[36] Luo K, Mao C, Zhuang Z, Fan J, Haugen NEL. A ghost-cell immersed boundary method for the simulations of heat transfer in compressible flows under different boundary conditions Part-II: complex geometries. Int J Heat Mass Transf 2017;104:98–111.
[37] Silva G. Consistent lattice Boltzmann modeling of low-speed isothermal flows at finite Knudsen numbers in slip-flow regime. II. Application to curved boundaries. Physical Review E 2018;98(2):023302.
[38] Sangani AS, Acrivos A. Slow flow past periodic arrays of cylinders with application to heat transfer. International journal of Multiphase flow 1982;8(3):193–206.
[39] Chai Z, Lu J, Shi B, Guo Z. Gas slippage effect on the permeability of circular cylinders in a square array. Int J heat and Mass Transf 2011;54(13–14):3009–14.
[40] Wang M, Wang J, Pan N, Chen S. Mesoscopic predictions of the effective thermal conductivity for microscale random porous media. Physical Review E 2007;75(3):036702.
[41] Xu K, Huang JC. A unified gas-kinetic scheme for continuum and rarefied flows. J Comput Phys 2010;229(20):7747–64.
[42] Shou D, Fan J, Ding F. Hydraulic permeability of fibrous porous media. Int J Heat Mass Transf 2011;54(17–18):4009–18.
[43] Borner A, Panerai F, Mansour NN. High temperature permeability of fibrous materials using direct simulation Monte Carlo. Int J Heat Mass Transf 2017;106:1318–26.
[44] Wu L, Ho MT, Germanou L, Gu XJ, Liu C, Xu K, et al. On the apparent permeability of porous media in rarefied gas flows. J Fluid Mech 2017;822:398–417.
[45] Succi S. Lattice boltzmann 2038. EPL (Europhysics Letters) 2015;109(5):50001.
[46] Zhao-Li G, Chu-Guang Z, Bao-Chang S. Non-equilibrium extrapolation method for velocity and pressure boundary conditions in the lattice Boltzmann method. Chinese Physics 2002;11(4):366.
[47] Succi S. Lattice boltzmann 2038. EPL (Europhysics Letters) 2015;109(5):50001.
[48] Wang P, Wang LP, Guo Z. Comparison of the lattice Boltzmann equation and discrete unified gas-kinetic scheme methods for direct numerical simulation of decaying turbulent flows. Physical Review E 2016;94(4):043304.
[49] Zhu L, Wang P, Guo Z. Performance evaluation of the general characteristics based off-lattice Boltzmann scheme and DUGKS for low speed continuum flows. J Comput Phys 2017;333:227–46.